

<https://doi.org/10.1038/s43247-024-01784-y>

Characterizing heatwaves based on land surface energy budget

Check for updates

Yinglin Tian^{1,2,3}, Axel Kleidon⁴, Corey Lesk^{5,6}, Sha Zhou⁷, Xiangzhong Luo⁸, Sarosh Alam Ghausi⁴, Guangqian Wang¹, Deyu Zhong¹ ✉ & Jakob Zscheischler^{2,9} ✉

Heat extremes pose pronounced threats to social-ecological systems and are projected to become more intense, frequent, and longer. However, the mechanisms driving heatwaves vary across heatwave types and are not yet fully understood. Here we decompose perturbations in the surface energy budget to categorize global heatwave-days into four distinct types: sunny-humid (38%), sunny-dry (26%), advective (18%), and adiabatic (18%). Notably, sunny-dry heatwave-days decrease net ecosystem carbon uptake by $0.09 \text{ gC m}^{-2} \text{ day}^{-1}$ over harvested areas, while advective heatwave-days increase the thermal stress index by 6.20 K in populated regions. In addition, from 2000 to 2020, sunny-dry heatwaves have shown the most widespread increase compared to 1979 to 1999, with 67% of terrestrial areas experiencing a doubling in their occurrence. Our findings highlight the importance of classifying heatwave-days based on their underlying mechanisms, as this can enhance our understanding of heatwaves and improve strategies for heat adaptation.

The increasing number of heat extremes, as well as the intensified frequency, duration, and intensity of heatwaves, stands out as one of the most significant facets of global warming.¹ This phenomenon poses a heightened threat to various aspects, including human health,² food production,³ plant carbon sequestration capabilities,⁴ and the functioning of essential infrastructure.⁵ In addition to the overall statistics, heatwaves present distinct social-ecological impacts,^{6–8} further complicating human adaptation to the warming climate. The previous study used the characteristics, e.g., humidity and intensity, of heatwaves to explain the direction, i.e., positive or negative, and the magnitude of their impact on plants and human health. Dry extreme events are frequently associated with dry soils and intensified land-surface interactions,⁹ thus reducing crop yields⁷ but relieving heat stress on humans.⁸ In contrast, humid heat is often linked to the onset of monsoon¹⁰ and may, to some extent, enhance crop production⁷ but lead to higher human mortality.¹¹ Moreover, heatwaves with high intensity are observed to be more likely to induce human mortality.⁶ It is therefore essential to categorize heatwaves and examine them individually.⁷

However, a classification based solely on heat characteristics (e.g., humidity and intensity) may prove inadequate, as it fails to consider the underlying drivers, and therefore would be difficult to explain the varying

impacts of heatwaves. The existing literature links the occurrence of extreme heat events to various energy-related drivers, including adiabatic heating, advective heating, and diabatic heating,¹² which in turn are influenced by large-scale circulation patterns and interactions between land and the atmosphere.¹³ Furthermore, both diabatic heating caused by land-atmosphere interaction⁹ and dry heat advection¹⁴ can induce a heatwave with low humidity. Nevertheless, the latter kind is not necessarily accompanied by decreased soil moisture and thus depressed vegetation production. Similarly, humid heat extremes can be attributed to different causes, including moist heat advection¹⁵ and solar radiation.¹⁶ Given that human heat stress is a function of air temperature, wind, radiation, and humidity,¹⁷ these two kinds of mechanisms may result in a differential human response to the humid heatwave. It is therefore essential to provide a quantitative description of the heat-generating mechanism and to undertake a subsequent classification of heatwaves.

Furthermore, the magnitude of heatwave frequency change has differed across regions in the historical period. West Europe, Mediterranean, and North Australia experienced the most significant increase in heatwave frequency over recent decades with a fixed threshold.^{18,19} The discrepancy in heatwave trends may be attributable to the differing heatwave mechanisms.

¹State Key Laboratory of Hydrosphere and Engineering, Key Laboratory of Hydrosphere Sciences of the Ministry of Water Resources, Department of Hydraulic Engineering, Tsinghua University, Beijing, China. ²Department of Compound Environmental Risks, Helmholtz Centre for Environmental Research-UFZ, Leipzig, Germany. ³Earth System Analysis, Potsdam Institute for Climate Impact Research (PIK) – Member of the Leibniz Association, Potsdam, Germany. ⁴Biospheric Theory and Modelling, Max Planck Institute for Biogeochemistry, Jena, Germany. ⁵Lamont-Doherty Earth Observatory, Columbia University, New York, USA. ⁶Department of Geography and Neukom Institute, Dartmouth College, Hanover, USA. ⁷State Key Laboratory of Earth Surface Processes and Resource Ecology, Faculty of Geographical Science, Beijing Normal University, Beijing, China. ⁸Department of Geography, National University of Singapore, Singapore, Singapore. ⁹Technische Universität Dresden, Dresden, Germany. ✉ e-mail: zhongdy@tsinghua.edu.cn; jakob.zscheischler@ufz.de

It has been demonstrated that the occurrence of compound hot and dry extreme events is determined by precipitation trends rather than temperature variation,²⁰ thereby implying disproportionate variations of different forms of heatwaves compared to the overall changes in heat extremes. In addition, global warming may alter atmospheric circulation²¹ and land-atmosphere interactions,²² which can generate heatwaves through differing mechanisms¹³ and might therefore lead to varying trends in heat extreme frequency. Hence, it is important to conduct individual investigations into the changes in heatwaves driven by different mechanisms.

In this paper, we cluster global summer heat extremes based on their primary drivers, which are identified based on a decomposition of temperature anomalies into the surface energy perturbation. A previous study has introduced a framework for quantifying the impact of adiabatic heating, advective heating, and diabatic heating on the occurrence of annual hottest days.¹² Expanding on it, the diabatic heating terms can be further subdivided into net shortwave radiation, downward longwave radiation, surface latent heat flux, surface sensible heat flux, and ground heat exchange, the relative importance of which varies depending on the region and the type of heatwave. For example, in Europe and the Tibetan Plateau, heatwaves are often attributed to increased solar radiation,^{16,23} whereas in the Arctic, high-temperature extremes are associated with positive anomalies in downward longwave radiation and enhanced heat advection from lower latitudes.^{15,24} Besides, the contribution of latent and sensible heat fluxes to temperature anomalies can differ between dry and humid heat waves.¹⁴ Given this complexity, here we adopt the full decomposition of temperature anomalies based on the surface energy balance to determine the dominant factors contributing to each heat extreme, which is then used to cluster heatwave-days at the global scale. Followingly, we investigate the mechanisms, impacts, and historical trends of the different types of heat extremes. To this end, we associate different types of heat extremes with hydro-meteorological variables including geopotential height, horizontal and vertical wind speed, cloud cover, and soil moisture, with a view to exploring the underlying mechanisms. And we compare the impacts of different kinds of heat extremes on ecosystems and human health by quantifying their effect on net carbon uptake and a thermal stress index. Finally, we present the frequency changes in the different types of heat extremes by comparing period of 2000–2020 and 1979–1999.

Results

Clustering heatwave-days based on the surface energy perturbations

We focus on heatwave-days, which are defined based on the 99th percentile threshold with a 15-day moving window. In the subsequent analysis, we only consider extensive ($>40,000 \text{ km}^2$) and persistent (≥ 6 days) heatwaves (see Methods: Identification of 3-dimensional heatwaves and definition of heatwave-days). Decomposing temperature anomalies of heatwave-days highlights geographical variations in the seven primary drivers (Supplementary Information Text S1), including surface advective heating (ΔT_{ADV}), surface adiabatic heating (ΔT_{ADIA}), surface net solar radiation (ΔT_{RS}), surface downward longwave radiation (ΔT_{RLD}), surface latent heat flux ($\Delta T_{\text{-LE}}$), surface sensible heat flux ($\Delta T_{\text{-H}}$), and ground heat flux (ΔT_{Q}) (see Methods: Decomposition of the temperature anomalies during heatwave-days and Supplementary Information Figs. S1–S3). Accordingly, the clustering of summer heatwave-days reveals four distinctive energy perturbation patterns (Fig. 1, see Methods: Clustering the heatwave-days based on energy perturbation). The number of four clusters emerges as the optimal number of clusters based on the Silhouette score²⁵ (Supplementary Information Fig. S4). Building upon the dominant surface energy input, the four types are referred to as “sunny-humid” (S-H), “sunny-dry” (S-D), “advective” (Adv), and “adiabatic” (Adia) heatwave-days, respectively.

Sunny-humid (S-H) heatwave-days account for 38% of all heatwave-days and are predominantly observed in high latitude and tropical regions, including Canada, Europe, Russia, Central South America, Central Africa, South China, and Southeast Asia (Fig. 1a). Sunny-humid heatwave-days are distinguished by substantial positive anomalies in surface solar radiation

and the offset effect of enhanced evaporative cooling (Fig. 1b). Sunny-dry (S-D) heatwave-days, representing 26% of all heatwave-days, are more frequently observed in subtropical regions, including south United States, Brazil, East and South Africa, India, North China, Southeast Asia, and North Australia (Fig. 1c). An increase in solar radiation is a defining feature of sunny-dry heatwave days, which is further amplified by a reduction in evaporation (Fig. 1d). Advective (Adv) and adiabatic (Adia) heatwave-days, each accounting for 18% of the total heatwave-days, are primarily caused by reinforced horizontal heat advection (Fig. 1f) and adiabatic heating (Fig. 1h), respectively. These two types, deviate from the aforementioned two types by exhibiting stronger anomalies in longwave radiation, rather than solar radiation. They are predominantly observed in extremely cold or arid areas, such as Greenland and the Sahara Desert (Fig. 1e, g). The robustness of our clustering was demonstrated through sensitivity analyses, which revealed that it remained consistent across a range of parameter specifications, thresholds, surface adiabatic and advective heating proxies, and clustering methods (Supplementary Information Text S2 and Figs. S4–S9).

The two sunny types (sunny-humid and sunny-dry) are located at humid, sub-humid, and semi-arid regions, with aridity index (defined as (Mean annual precipitation)/(Mean annual potential evapotranspiration)) exceeding 0.2 in the majority of cases, while advective and adiabatic heatwave-days generally occur at arid or hyper-arid regions (Fig. 1i, j). Furthermore, the sunny-humid type is more prevalent in regions with higher humidity than the sunny-dry type. In contrast, the latter is more prevalent in areas exhibiting a higher correlation between summer temperature (T2m) and soil moisture (SM) anomaly (Fig. 1k, l).

Mechanisms and social-ecological impacts of the four types of heatwave-days

The distinction in the surface energy perturbation contributions for the four heatwave categories is further associated with the varying hydro-meteorological conditions (see Methods: Composite analysis and significant test). While all four heat wave types occur during high-pressure systems (Fig. 2a), only sunny-humid and sunny-dry heatwave-days are characterized by a significant reduction in cloud cover (Fig. 2b), which leads to positive anomalies in shortwave radiation and triggers the two sunny-type heat extremes (Supplementary Information Fig. S10a, b). Despite the similar atmospheric settings, the two sunny types of heatwave-days are further distinguished from each other by the amplifier, i.e., the surplus term in the surface energy perturbation to sustain the heat extremes. During sunny-humid heatwave-days, the enhancement of solar radiation is sufficient to contribute to the heat storage of the boundary layer, thereby increasing the downward longwave radiation and maintaining the high temperature after lag 0 (Supplementary Information Fig. S10a). Nevertheless, during sunny-dry heatwave-days, the high temperature is sustained and amplified by the negative anomalies in latent heating (i.e., an increase in -LE) (Supplementary Information Fig. S10b), which is further caused by a more pronounced decrease in soil moisture (Fig. 2c) and supplements the relatively slight variation in geopotential height (Fig. 2a). In contrast, advective heatwave-days are distinguished by positive horizontal heat advection near the surface due to an increase in temperature gradient (Fig. 2d) and stronger surface wind speeds (Fig. 2e). Adiabatic heatwave-days are accompanied by intensified subsidence of air, as shown by the downward triangles in Fig. 2f. Furthermore, the heat advection and adiabatic heating result in increased heat storage in the boundary layer simultaneously, thus promoting the enhancement in downward longwave radiation as the amplifier of advective and adiabatic heatwave-days (Supplementary Information Fig. S10c, d).

While the present study is primarily concerned with the mechanisms involved, the impact analysis serves to further distinguish the four identified heatwave types. Accordingly, an investigation is conducted into the impacts of the four identified types of heatwave-days on ecosystems and thermal stress on humans. We have limited our consideration to locations that have experienced all four types of heatwaves during the period 1979–2020 to

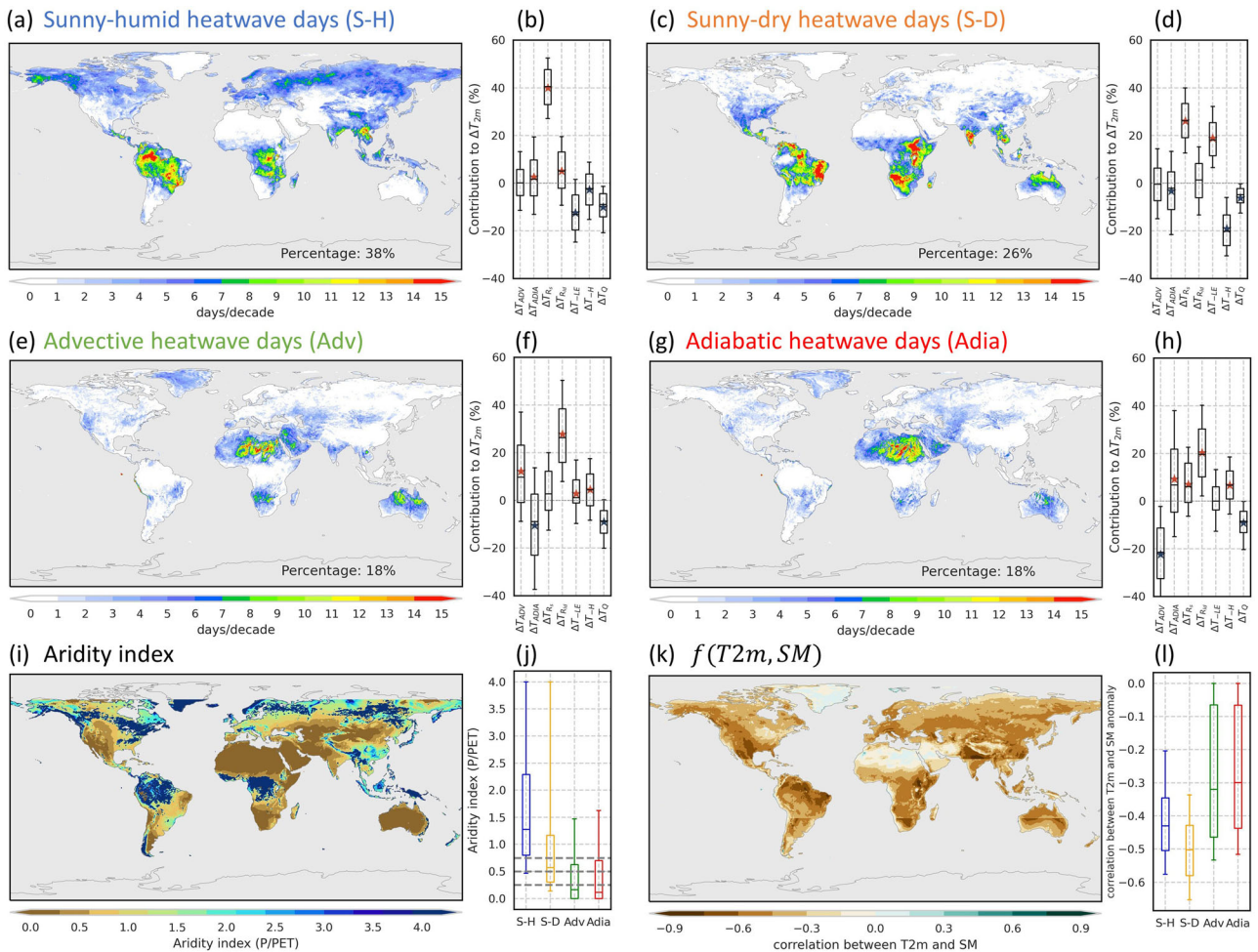


Fig. 1 | Distribution of four kinds of heatwave-days and the corresponding energy perturbation patterns. **a, c, e, and g** Distribution of frequency and **(b, d, f, and h)** the corresponding energy perturbation distributions for **(a, b)** sunny-humid, **(c, d)** sunny-dry, **(e, f)** advective, **(g, h)** adiabatic heatwave-days. **i, k** Distribution of aridity index (multi-year mean precipitation divided by multi-year mean potential evaporation) and $f(T2m, SM)$ (Pearson correlation coefficient between summer temperature and soil moisture anomaly). **j, l** Aridity index and $f(T2m, SM)$ of the four types of the heatwave-days. In panels **a, c, e, g, i** and **k**, the grey mask is the area excluded in this study, i.e., marine region and the Antarctica. In panels **b, d, f, h, j** and **l**, the boxplot shows the median of and spread among the heatwave-days inside the clustering, with the box representing the interquartile range and the whiskers representing the 95th and 5th percentiles; stars denote mean values that are

significantly different from normal conditions ($p < 0.01$), with the red ones higher than zero and the blue ones lower. In panel **j**, the dashed lines indicate 0.75, 0.5, and 0.25, which divides the regions into humid, subhumid, subarid, and arid regions. ΔT_{ADV} , ΔT_{ADIA} , ΔT_{RS} , ΔT_{RD} , ΔT_{-LE} , ΔT_{-H} , and ΔT_Q are the contribution of advective heating, adiabatic heating, net surface solar radiation, downward longwave radiation, surface latent heat flux, surface sensible heat flux, and the ground heat flux to the temperature anomalies during heatwave-days. Note that for each heatwave day, the energy perturbation array $[[\Delta T_{ADV}, \Delta T_{ADIA}, \Delta T_{RS}, \Delta T_{RD}, \Delta T_{-LE}, \Delta T_{-H}, \Delta T_Q]]$ are normalized by their Manhattan norm, i.e., dividing each term in the array by the sum of the absolute values, to make the values comparable among heatwave-days while keeping relative magnitude and signs within each heatwave-day (Supplementary Information Text S3).

exclude the influence of the geographical locations (see Methods: Composite analysis and significant test and Supplementary Information Fig. S11). As shown in Fig. 3a, the net ecosystem carbon uptake ($-NEE$) is diminished by $0.06 \text{ gC m}^{-2} \text{ day}^{-1}$ during sunny-dry heatwave-days ($0.09 \text{ gC m}^{-2} \text{ day}^{-1}$ over harvested area). The most pronounced declines in $-NEE$ are observed in the southeastern United States, western Russia, north-eastern China, Brazil, Central and South Africa, and northern Australia, reaching up to $0.1 \text{ gC m}^{-2} \text{ day}^{-1}$ (Supplementary Information Fig. S12). The decrease in $-NEE$ is attributable to a greater decline in gross primary productivity (GPP) than in total ecosystem respiration (TER). GPP is observed to decrease by approximately $0.12 \text{ gC m}^{-2} \text{ day}^{-1}$ (Fig. 3b) during sunny-dry heatwave-days ($0.16 \text{ gC m}^{-2} \text{ day}^{-1}$ over harvested area) due to the concurrence of high temperatures and low soil moisture (Fig. 2c), subjecting the plants to both thermal and water stress. High temperatures suppress TER by about $0.06 \text{ gC m}^{-2} \text{ day}^{-1}$ ($0.07 \text{ gC m}^{-2} \text{ day}^{-1}$ over harvested area) during sunny-dry days (Fig. 3c), which is approximately half of the reduction in GPP . Although reduced TER serves to compensate for the weakening of GPP ,

thereby alleviating the decrease in carbon uptake, it nevertheless indicates an overall suppression of vegetation growth during the sunny-dry heatwave-days.

While sunny-dry heatwave-days have the most detrimental impact on plant productivity, they have the least influence on human thermal stress (Fig. 3d~f). When all locations that have experienced all four types of heatwaves are considered, advective heatwave-days have the greatest impact on human thermal stress. However, the differences among the four types are relatively minor (as illustrated by the solid boxplot in Fig. 3d). When the analysis is restricted to populated areas (population density ≥ 1 person km^{-2}), advective heatwave-days show a more pronounced positive TSI anomalies, with a mean value reaching 6.20 K (dashed boxplot in Fig. 3d). In regions such as Canada, Russia, Inner Mongolia, and the south coast of Australia, TSI anomalies even exceed 10.0 K (Supplementary Information Fig. S13). The detrimental impact of advective heatwave-days on human thermal stress primarily result from the combination of high dry-bulb temperature and relative humidity (Fig. 3e, f).

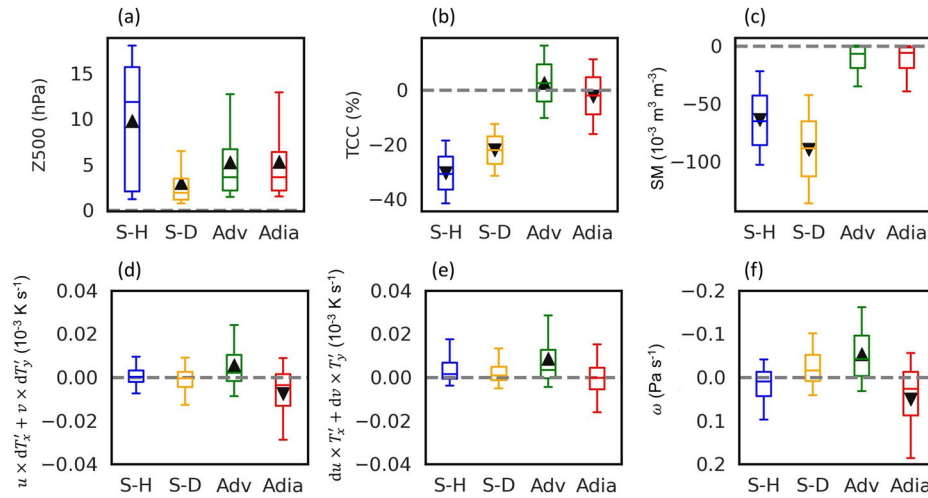
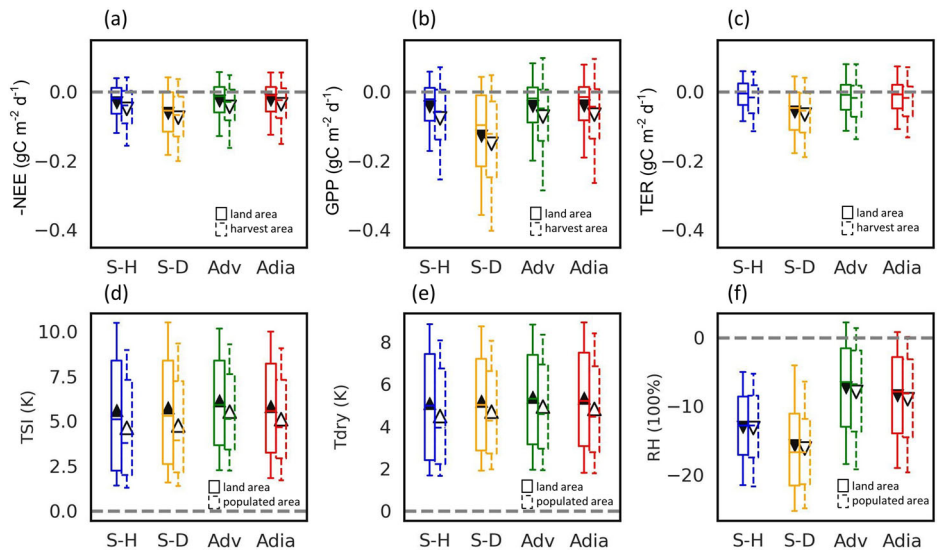


Fig. 2 | Mechanisms of four kinds of summer heatwave-days. Anomalies of (a) geopotential height on 500 hPa, (b) total cloud cover fraction, (c) surface soil moisture, (d) near-surface heat advection rate due to the anomalous horizontal temperature gradient, (e) near-surface heat advection rate due to anomalous horizontal wind speed, and (f) vertical velocity for sunny-humid (S-H), sunny-dry (S-D), advective (Adv), and adiabatic (Adia) heatwave-days. The boxplot shows the median of and spread among the heatwave-days inside the clustering, with the box representing the interquartile range and the whiskers representing the 95th and 5th

percentiles. In Panels d and e, u and v are zonal and meridional wind speed, T'_x and T'_y are zonal and meridional temperature gradients, and d represents deviation from climatology; the near-surface proxy is calculated in a similar way as near-surface advective and adiabatic heating (see Methods: Decomposition of the temperature anomalies during heatwave-days). Triangles denote mean values significantly different from normal conditions ($p < 0.01$), with the upward ones presenting positive and the downward ones negative, except Panel f, where the upward and downward triangles present anomalous ascent and descent of the air, respectively.

Fig. 3 | Impacts of four kinds of summer heatwave-days on ecology and humans. Anomalies of (a) gross primary productivity (GPP), (b) terrestrial ecosystem respiration (TER), (c) carbon uptake (-NEE, i.e., the negative value of net ecosystem exchange), (d) thermal stress index (TSI), (e) dry temperature (T_{dry}), and (f) relative humidity (RH) for sunny-humid (S-H), sunny-dry (S-D), advective (Adv), and adiabatic (Adia) heatwave-days. In Panels a, b and c, dashed boxplot represents the results over harvest area (crop area fraction > 0). In Panels d, e and f, dashed boxplot represents the results over populated area (population density > 1 person km^{-2}). The boxplot shows the median of and spread among the heatwave-days inside the clustering, with the box representing the interquartile range and the whiskers representing the 95th and 5th percentiles. Triangles denote mean values that are significantly different from normal conditions ($p < 0.01$), with the upward ones presenting positive and the downward ones negative. And all variables are detrended.



Historical changes in occurrence of summer heatwave-days

To investigate historical changes, we present the differences in the frequency of four types of heatwave-days between the 2000–2020 period and the 1979–1999 period in Fig. 4. With the mean temperature shifts to a warmer level, the frequency of all four types of the heatwave-days have increased. However, the hotspot and the increasing rate vary. The most widespread increase is observed in the frequency of sunny-dry heatwave days. Figure 4a demonstrates that approximately 67%, 54%, and 46% of the land area have experienced increases of 1, 2, and 3 times, respectively, in sunny-dry heatwave days. The regions exhibiting the greatest increase in sunny-dry heatwave days are those that are semi-humid and semi-arid (Fig. 4c). These regions also demonstrate a high correlation coefficient between temperature and soil moisture (Fig. 1k), including the southern United States, western Europe, north-eastern China, central and south-east Asia, East Africa,

south-west India, South Asia, and north-east Australia. Additionally, 60% (51% and 44%) of the land area has experienced 1 (2 and 3) times more sunny-humid heatwave-days, located in humid and semi-humid regions, including west Canada, west Europe, east Eurasia, west South America, central Africa, South Asia and southeast Asia (Fig. 4b). Moreover, 60% (51% and 44%) and 51% (44% and 38%) of the land area has experienced 1 (2 and 3) times more advective and adiabatic heatwave days, respectively. These increases are typically observed in regions with low temperatures and high aridity (Fig. 4d, e).

Since a lack of preparedness can intensify the impacts of heatwaves, Fig. S14 (in Supplementary Information) highlights the newly affected locations of the four types of heatwave-days, i.e., where the heatwave-days only occur during 2000–2020 but not present during 1979–1999 ($Frequency_{HW\ type, 1979-1999} = 0$). Approximately 27% of the land area (30%

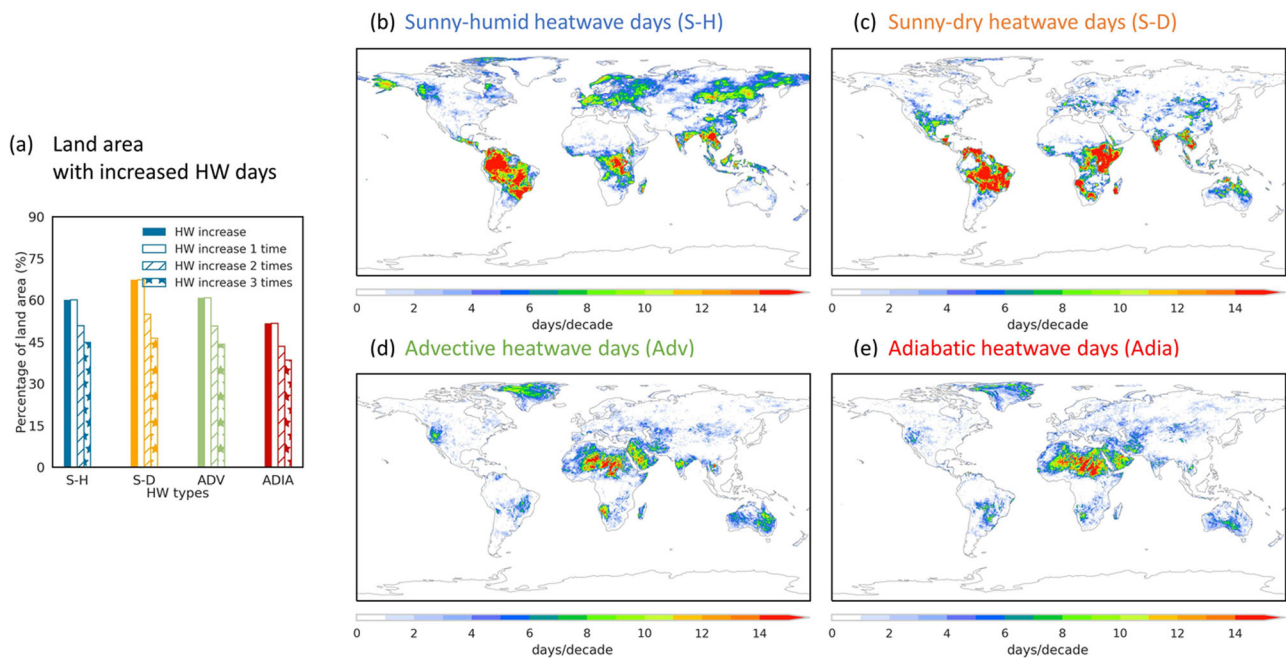


Fig. 4 | Historical changes in frequency of the four types of heatwave-days. a Percentage of the land area experiencing 1–3 times increase of the four types of the heatwave-days during 2000–2020 period compared with 1979–1999 period.

b–e Distribution of the difference in frequency of the four types of heatwave-days between 2000–2020 period and 1979–1999 period.

of populated regions) began to encounter advective heatwave-days only after 2000, which is the largest among the four types. Approximately 26% of the land area (29% of populated regions) only began to experience adiabatic heatwave-days after 2000. The newly affected locations for both advective and adiabatic heatwave days are distributed globally, with Greenland exhibiting the most pronounced increase. Additionally, approximately 18% of the land area (22% of populated regions) began to experience sunny-humid heatwave-days only after 2000, and about 24% of the land area (26% of populated regions) started to experience sunny-dry heatwave-days in the same period. The newly affected locations for sunny-humid heatwave-days are predominantly located in the subtropics, with Central America, Central Europe, Inner Mongolia, and Southeast Asia representing significant hot-spots. The majority of mid- and high-latitude regions have been affected by sunny-dry heatwaves, with the most pronounced increase occurring in Central South America, Western Europe, the Mediterranean, Central Africa, and North-Eastern China.

Discussion

We have analyzed temperature anomalies of terrestrial summer heatwave-days during 1979–2020 and categorized heatwave-days into four types based on the contributions of surface energy perturbations. As shown in Fig. 5, sunny-humid and sunny-dry heatwave-days are accompanied by high pressure and less cloud, with sunny-dry ones amplified by less soil moisture. Advective and adiabatic heatwave-days are caused by anomalies in the horizontal heat advection and vertical air movement, respectively, and are strengthened by increased downward longwave radiation. Among the four types, sunny-dry heatwave-days cause the most harm to ecosystem production in harvested regions. Meanwhile, the advective type has the greatest impact on human thermal stress in populated areas. Compared to 1979–1999, 67% of terrestrial areas experienced a doubling sunny-dry heatwave day during 2000–2020. Additionally, 27% of terrestrial areas only began to experience advective heatwaves after 2000.

The observed prevalence of adiabatic heating in mountainous areas and advective heating along the coast and high-latitude regions aligns with the previous findings.¹² However, inconsistencies emerge in mid-latitude regions. This discrepancy can be attributed to our focus on large three-dimensional heatwaves defined by maximum daily temperature and the

calculation of climatology over a 42-year period, which differs from the existing literature that targeted at the days with the highest annual daily mean temperature and computed climatology over a four-year period before and after.¹² Furthermore, our specific emphasis on large spatio-temporal contiguous heatwaves may contribute to a reduction in humid extremes (Fig. 4f), which is consistent with the previous finding that the compound hot-dry events have a larger heat intensity than heatwaves alone.²⁶ Our findings reinforce the notion that three-dimensional (spatio-temporal) heatwaves possess distinctive drivers and characteristics when compared to one-dimensional high-temperature days. This underscores the necessity for the analysis of spatio-temporal dimensional heatwaves, particularly those of considerable intensity, given their more pronounced spatial and temporal cumulative impacts.²⁷

Additionally, discrepancies may emerge from the differentiation between Eulerian and Lagrangian methodologies. A Lagrangian analysis offers a more detailed history of the heatwave event, particularly for events with long Lagrangian lifetimes. Nevertheless, the decomposition of temperature anomalies into seven energy perturbations as in this study with a Lagrangian analysis would necessitate the interpolation of all related variables from grid-point datasets onto trajectories. This could introduce bias and increase the computational complexity. Moreover, the Eulerian approach can still capture relevant aspects of the history of air parcels. For example, it can identify whether air parcels have been pre-heated prior to reaching the target location, where warmer parcels contribute a greater amount of downward longwave radiation towards the surface.²⁸ Accordingly, the Eulerian method is employed in this study to achieve an optimal balance between computational efficiency and the provision of meaningful insights into the thermal dynamics of heatwave events.

Our study provides insights into the changes in heatwave-days, suggesting that these changes may result not only from variations in individual drivers but also from the interactions between compounding drivers. It is, therefore, intriguing to further explore the interaction between the compound driver. In the case of sunny-dry heatwave-days, the relationship between anomalies in the compounding drivers, solar radiation and latent heat flux, may be influenced by the correlation between variations in cloud cover and soil moisture²⁹ and land-air interaction.⁹ In the case of sunny-humid, advective, and adiabatic heatwave-days, the triggering components




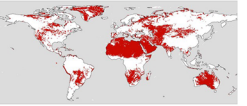
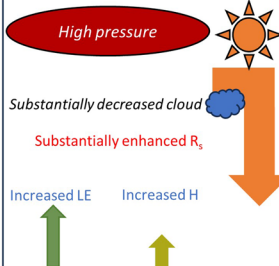
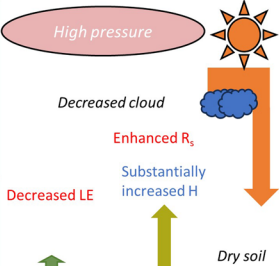
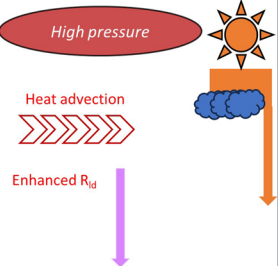
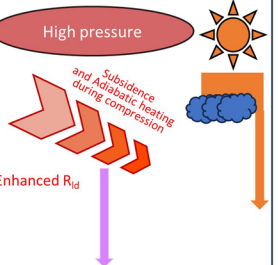


Clustering	Sunny-humid heatwave-days	Sunny-dry heatwave-days	Advection heatwave-days	Adiabatic heatwave-days
Percentage	38%	26%	18%	18%
Hotspot				
Mechanism				
Detrimental impact (strongest)				

Fig. 5 | Summary of the proportion, hotspots, mechanism, and impact for four kinds of summer heatwave-days. In row “Hotspot”, locations where the frequency exceeds 5 days per decade, as depicted in Fig. 1, are marked. In row “Mechanism”, the arrow direction relates to the corresponding terms in the surface energy balance,

with red text identifying dominant surface energy inputs contributing to high temperatures, and the darker the color of “High pressure” ellipse is, the higher the corresponding anomaly is. In row “Detrimental impact”, icons indicate the strongest impactful type on ecosystem or human thermal stress.

are solar radiation, heat advection, and adiabatic heating, respectively, while all the amplifiers are downward longwave radiation. This can be understood by the semi-empirical formula of downward longwave radiation,²⁸ which reveals that downward longwave radiation is sensitive to heat storage and humidity of the air column. The radiative kernel, representing the sensitivity of downward longwave radiation changes to temperature, humidity, and cloud cover, has been observed to increase on a global scale.³⁰ This can partly contribute to the increase of the sunny-humid, advective, and adiabatic heatwave-days.

In conclusion, our research emphasizes the importance of categorizing heat extremes based on their varying underlying mechanisms. This can help to improve the representation of heatwaves in climate models, therefore contributing to more robust societal adaptation to increasing temperature. We identify varying geographical distributions and impacts of the different types of heat extremes, which underscore the necessity for a region-specific approach when addressing distinct heat-related risks. Additionally, we highlight different historical trends in heatwave-days, particularly the most widespread increase in sunny-dry heatwave-days and the largest new-affected area of advective heatwaves, which implies additional heat stress on terrestrial ecosystems and human being health.

Materials and methods

Data

The ERA5³¹ reanalysis datasets during the period of 1979–2020 are employed in this study. In the ERA5-single-level dataset, the following variables are downloaded: daily maximum air temperature (T_{max}), daily mean (average of hourly data) of surface temperature (T_s), 2 m air temperature (T_{2m}), surface net solar radiation (R_s), surface downward longwave radiation (R_{ld}), surface latent heat flux (LE), surface sensible heat flux (H), total cloud cover (TCC), surface soil moisture (SM), surface pressure (P_s), relative humidity (RH), and universal thermal climate index (TSI).¹⁷ In the ERA5-pressure-level dataset, the following variables are downloaded: geopotential height at 500 hPa (Z_{500}), air temperature (T_{pl}), horizontal wind speed (u_{pl} and v_{pl}), and vertical velocity (ω_{pl}) on 950 hPa, 850 hPa, 750 hPa, and 650 hPa. The spatial resolution is $0.25^\circ \times 0.25^\circ$. It should be noted that R_s and R_{ld} are positive downward (from the air to the land surface), while LE and H are positive upward (from the land surface to the air).

FLUXCOM^{32,33} monthly estimates (with climate data input from the ERA5 dataset) of gross primary productivity (GPP), terrestrial ecosystem respiration (TER), and net ecosystem exchange (NEE) are downloaded and regridded to a resolution of $0.25^\circ \times 0.25^\circ$ from a resolution of $0.5^\circ \times 0.5^\circ$. As the FLUXCOM dataset spans the period from 2001 to 2015, the impact of heatwave-days on the ecosystem is presented for these 16 years only. In order to consider vulnerability, crop area fraction³⁴ and the Gridded Population of the World (GPW) population density data³⁵ are also used in this analysis.

Identification of 3-dimensional heatwaves and definition of heatwave-days

The analysis is focused on summer terrestrial heatwaves. The data employed for the temperate zone in the Northern and Southern Hemispheres ($23.5^\circ N$ – $90^\circ N$ and $23.5^\circ S$ – $60^\circ S$, respectively) encompass the months of JJA (June, July, August) and DJF (December, January, February). The entirety of the data set, spanning 12 months, is employed for the tropical region ($23.5^\circ N$ – $23.5^\circ S$).

Three-dimensional (3-D) heatwaves are contiguous in three dimensions, namely time, latitude, and longitude.³⁶ To identify the 3-D heatwaves over the terrestrial region, we initially select days with daily maximum temperature (T_{max}) exceeding the corresponding 15-day moving 99th percentile for each calendar day and each grid ($T_{max,99th}$) as hot days. Subsequently, the 3-D connected component (CC3D) algorithm (<https://pypi.org/project/connected-components-3d20>), with a connectivity of 6, is employed to define hot days that are spatiotemporally connected as hot cells. Ultimately, the selection is made of those hot cells that persist for a minimum of 6 consecutive days and encompass an area of more than $40,000 \text{ km}^2$. These are then classified as terrestrial summer heatwaves.¹⁹ The days included in the identified heatwaves are referred to as heatwave-days.

In total, 3454 heatwaves (HW) were identified, encompassing 8,463,177 heatwave-days (HW-days).

Decomposition of the temperature anomalies during heatwave-days

To decompose temperature anomalies, we first remove the seasonal cycle by subtracting the multi-year average for each calendar day for all related

variables. In statistical terms, an anomaly represents a deviation from the multi-year average of a given calendar day.

Temperature anomalies are decomposed as follows,

$$\Delta T_{2m} = \Delta T_{advection} + \Delta T_{adiabatic} + \Delta T_{diabatic}, \quad (1)$$

where ΔT_{2m} represents the anomaly of 2 m air temperature, the three terms on the right side of Eq. (1) are the contributions of advective, adiabatic, and diabatic heating.¹²

To estimate anomalies in near-surface advective and adiabatic heating term on the heatwave-days ($\Delta T_{advection}$ and $\Delta T_{adiabatic}$), we first calculate the advective and adiabatic heating anomaly on different pressure layers, including 950 hPa, 850 hPa, 750 hPa, and 650 hPa as follows,

$$\Delta T_{advection,pl} = -\left(\frac{\partial T_{pl}}{\partial x} u_{pl} + \frac{\partial T_{pl}}{\partial y} v_{pl}\right) \Delta t, \quad (2)$$

$$\Delta T_{adiabatic,pl} = \left(\frac{\kappa T_{pl}}{p_s} - \frac{\partial T_{pl}}{\partial p}\right) \omega_{pl} \Delta t, \quad (3)$$

where pl is the index of air pressure level; $\kappa = 0.286$ is Poisson constant; p_s is surface pressure; T_{pl} , u_{pl} , v_{pl} , and ω_{pl} are air temperature, eastward wind velocity, northward wind velocity, and vertical wind velocity at the pressure level, respectively. The time step, denoted by Δt , is equal to one day, as the data employed are daily reanalysis data.

Advective (adiabatic) heating anomalies at 950 hpa were used for heatwave days where surface pressure ranges from 900 to 1100 hpa. This accounts for 87% of total heatwave days and is demonstrated in Figs. S2, S3 (in Supplementary Information). Similarly, the advective (adiabatic) heating anomaly on 850 hPa, 750 hPa, and 650 hPa are used for the heatwave-days with surface pressure ranging between 800–900 hPa (10% of heatwave-days), 700–800 hPa (2% of heatwave-days), and 500–700 hPa (1% of heatwave-days), i.e.,

$$\Delta T_{advection} = \begin{cases} \Delta T_{advection,950hPa} (p_s \geq 900hPa) \\ \Delta T_{advection,850hPa} (900hPa > p_s \geq 800hPa) \\ \Delta T_{advection,750hPa} (800hPa > p_s \geq 700hPa) \\ \Delta T_{advection,650hPa} (p_s < 700hPa) \end{cases} \quad (4)$$

$$\Delta T_{adiabatic} = \begin{cases} \Delta T_{adiabatic,950hPa} (p_s \geq 900hPa) \\ \Delta T_{adiabatic,850hPa} (900hPa > p_s \geq 800hPa) \\ \Delta T_{adiabatic,750hPa} (800hPa > p_s \geq 700hPa) \\ \Delta T_{adiabatic,650hPa} (p_s < 700hPa) \end{cases} \quad (5)$$

In this way, we get the near-surface advective and adiabatic heating anomaly (Supplementary Information Figs. S2g, S3g), which is then used for clustering.

To estimate diabatic heating, we used the anomalies in the skin temperatures as

$$\Delta T_{diabatic} = f \Delta T_s, \quad (6)$$

where f represents the ratio between air temperature changes resulting from diabatic forcing ($\Delta T_{diabatic}$) and skin temperature changes (ΔT_s), and it has typically been assumed to be 1 in previous studies.^{16,37,38} Our analysis, as depicted in Fig. S5 (in Supplementary Information), yields $f = 0.91$ when considering all the detected heatwave-days during the summer period from 1979 to 2020. The clustering results with $f = 1$ are presented in the main text (Fig. 1), while Fig. S6 (in the Supplementary Information) demonstrates that the clustering remains unchanged when using $f = 0.91$. With Eq. (6), we can further attribute $\Delta T_{diabatic}$ to anomalies in the surface energy balance, which

can be written as follows:

$$R_s + R_{ld} - R_{lu} - LE - H = Q. \quad (7)$$

Here R_s is the net surface solar radiation, R_{ld} is the downward flux of longwave radiation, R_{lu} is the emitted upward flux of longwave radiation, LE is surface latent heat flux, H is surface sensible heat flux, and Q the ground heat flux. Note that the radiation terms are downward positive and turbulent heat flux is upward positive. By using $R_{lu} = \sigma T_s^4$ (with σ being the Stefan-Boltzmann constant) and differentiating Eq. (7), we can express ΔT_s as

$$\Delta T_s = \frac{\Delta R_s + \Delta R_{ld} - \Delta LE - \Delta H - \Delta Q}{4\sigma \bar{T}_s^3}. \quad (8)$$

Taking Eq. (6) and Eq. (8) into Eq. (1), ΔT_{2m} can be decomposed as

$$\Delta T_{2m} = \Delta T_{adiabatic} + \Delta T_{advection} + \frac{\Delta R_s}{4\sigma \bar{T}_s^3} + \frac{\Delta R_{ld}}{4\sigma \bar{T}_s^3} + \frac{-\Delta LE}{4\sigma \bar{T}_s^3} + \frac{-\Delta H}{4\sigma \bar{T}_s^3} + \frac{-\Delta Q}{4\sigma \bar{T}_s^3}. \quad (9)$$

In this way, the changes in the air temperature can be attributed to the seven components represented by terms on the right-hand of Eq. (9). This yields an energy perturbation array, i.e., $[\Delta T_{adiabatic}, \Delta T_{advection}, \frac{\Delta R_s}{4\sigma \bar{T}_s^3}, \frac{\Delta R_{ld}}{4\sigma \bar{T}_s^3}, \frac{-\Delta LE}{4\sigma \bar{T}_s^3}, \frac{-\Delta H}{4\sigma \bar{T}_s^3}, \frac{-\Delta Q}{4\sigma \bar{T}_s^3}]$, for every heatwave-day.

Clustering the heatwave-days based on energy perturbation

To identify the various mechanisms underlying the occurrence of heatwaves, we conducted an unsupervised clustering analysis of the similar patterns observed across the energy perturbation array, i.e., $[\Delta T_{adiabatic}, \Delta T_{advection}, \frac{\Delta R_s}{4\sigma \bar{T}_s^3}, \frac{\Delta R_{ld}}{4\sigma \bar{T}_s^3}, \frac{-\Delta LE}{4\sigma \bar{T}_s^3}, \frac{-\Delta H}{4\sigma \bar{T}_s^3}, \frac{-\Delta Q}{4\sigma \bar{T}_s^3}]$. We adopt K-means³⁹ to perform clustering, with the energy perturbation array normalized by their Manhattan norm,²⁵ i.e., dividing each term in the array by the sum of the absolute values, with the objective of ensuring comparability across heatwave-days while maintaining the relative magnitude and signs within each heatwave-day (Supplementary Information Text S3).

The optimal number of clusters was identified based on Silhouette index.⁴⁰ The Silhouette index is defined as the degree of proximity between each point within a given cluster and points in neighboring clusters, with a range of -1 to 1 . A value of the Silhouette Index approaching 1 indicates that the clusters are more distinct and well-separated. A value approaching 0 indicates that the clusters are in close proximity or overlapping, whereas negative values suggest that the data points may have been erroneously assigned to an incorrect cluster.

Composite analysis and significant test

To investigate the mechanisms and impacts of the heatwave days, a composite analysis is employed. Prior to conducting the composition, the seasonal cycle is removed in the same way introduced above for all the related variables. The impact-related variables depicted in Fig. 3, including GPP , TER , $-NEE$, TSI , dry-bulb temperature (T_{dry}), and relative humidity (RH), are linearly detrended to remove long-term trends, as the focus of this study is on the impacts of short-term variability.

For the monthly data, i.e., GPP , TER , and $-NEE$, it is possible that a specific time step (at a monthly scale) at a given grid point may be associated with multiple types of heatwave-days (at a daily scale). To clearly show the impacts of the four types of heatwave-days on ecosystems, we exclude months when at least two types of heatwave-days coincide with each other.

To remove the influence of the geographical locations on the impact analysis, we have only considered those locations that have experienced all four types of heatwaves during the period 1979–2020 (Supplementary

Information Fig. S11), which accounts for 37% of the land area. To incorporate vulnerability into the analysis, we present the results of a composite analysis of the impact on ecosystems within the harvest area (crop area fraction >0) and a composite analysis of the impact on human thermal stress within populated regions (population density >=1 person per km²) in dashed boxplots in Fig. 3 and contours in Figs. S12, S13 (in Supplementary Information).

The significance test is performed following previous study.⁴¹ The “control” estimate is established separately for four categories of heatwave days, with consideration given to the corresponding geographical distributions of frequency (Fig. 1). In the case of sunny-humid heatwave-days, one synthetic set is generated by randomly perturbing the summertime days while maintaining the same geographical distributions of frequency observed in the original data set (Fig. 1a). Subsequently, variables related to surface energy perturbations, mechanisms, and impacts are then averaged over the aforementioned synthetic set, thereby obtaining composite “control” values. To perform the significance test for monthly data, the monthly-scale synthetic set is generated, with the months being randomly selected. The entire “control” estimate is composed of 1000 composited “control” values, generated through the repetition of the entire process 1000 times. A 99% significance level is then attained if the true composited values for the corresponding heatwave-days fall outside the top or bottom 0.5% percentile of the 1000 composited “control” estimates.

Reporting summary

Further information on research design is available in the Nature Portfolio Reporting Summary linked to this article.

Data availability

Data presented in this manuscript are available through the Copernicus Climate Change Service Climate Data Store (CDS, <https://doi.org/10.24381/cds.adbb2d47>, <https://doi.org/10.24381/cds.bd0915c6>, and <https://doi.org/10.24381/cds.553b7518>) for ERA5 reanalysis data, Data Portal of the Max Planck Institute for Biogeochemistry (https://doi.org/10.17871/FLUXCOM_RS_METEO_CRUNCEPv6_1980_2013_v1) for FLUXCOM carbon flux data, NASA Socioeconomic Data and Applications Center (SEDAC, <https://doi.org/10.7927/H4F47M65>) for population density data, and MIRCA2000 for harvest area data.

Code availability

All the codes and data to produce the main figures are available via https://github.com/tiany97/HW_cluster and <https://doi.org/10.5281/zenodo.13869812>.

Received: 18 March 2024; Accepted: 11 October 2024;

Published online: 24 October 2024

References

- IPCC, 2023: Climate Change 2023: Synthesis Report. *Contribution of Working Groups I, II and III to the Sixth Assessment Report of the Intergovernmental Panel on Climate Change* (eds Core Writing Team, H. Lee and J. Romero). (IPCC, Geneva, Switzerland, 2023), <https://doi.org/10.59327/IPCC/AR6-9789291691647>.
- Raymond, Colin et al. The emergence of heat and humidity too severe for human tolerance. *Sci. Adv.* **6**, eaaw1838 (2020).
- Lesk, C. et al. Compound heat and moisture extreme impacts on global crop yields under climate change. *Nat. Rev. Earth Environ.* **3**, 872–889 (2022).
- Van der Woude, A. M. et al. Temperature extremes of 2022 reduced carbon uptake by forests in Europe. *Nat. Commun.* **14**, 6218 (2023).
- Forzieri, G. et al. Escalating impacts of climate extremes on critical infrastructures in Europe. *Glob. Environ. Change* **48**, 97–107 (2018).
- Royé, D., Codesido, R., Tobias, A. & Taracido, M. Heat wave intensity and daily mortality in four of the largest cities of Spain. *Environ. Res.* **182**, 109027 (2020).
- Ting, M. et al. Contrasting impacts of dry versus humid heat on US corn and soybean yields. *Sci. Rep.* **13**, 710 (2023).
- Wouters et al. Soil drought can mitigate deadly heat stress thanks to a reduction of air humidity. *Sci. Adv.* **8**, eabe6653 (2022).
- Bartusek, S., Kornhuber, K. & Ting, M. North American heatwave amplified by climate change-driven nonlinear interactions. *Nat. Clim. Change* **12**, 1143–1150 (2022).
- Wehner, M., Stone, D., Krishnan, H., AchutaRao, K. & Castillo, F. The deadly combination of heat and humidity in India and Pakistan in Summer 2015. *Bull. Am. Meteor. Soc.* **97**, S81–S86 (2016).
- Rogers, C. D. W. et al. Recent increases in exposure to extreme humid-heat events disproportionately affect populated regions. *Geophys. Res. Lett.* **48**, e2021GL094183 (2021).
- Röthlisberger, M. & Papritz, L. Quantifying the physical processes leading to atmospheric hot extremes at a global scale. *Nat. Geosci.* **16**, 210–216 (2023).
- Domeisen, D. I. V. et al. Prediction and projection of heatwaves. *Nat. Rev. Earth Environ.* **4**, 36–50 (2023).
- Ha, K. J. et al. Dynamics and characteristics of dry and moist heatwaves over East Asia. *NPJ Clim. Atmos. Sci.* **5**, 49 (2022).
- Tian, Y. et al. Atmospheric energy sources for winter sea ice variability over the North Barents–Kara Seas. *J. Clim.* **35**, 5379–5398 (2022).
- Tian, Y. et al. Radiation as the dominant cause of temperature extremes on the Tibetan Plateau. *Environ. Res. Lett.* **18**, 074007 (2023a).
- Di Napoli C., Barnard C., Prudhomme C., Cloke H. L. and Pappenberger F. (2020) *Thermal comfort indices derived from ERA5 reanalysis* (Copernicus Climate Change Service (C3S) Climate Data Store (CDS), accessed 01 October 2023); <https://doi.org/10.24381/cds.553b7518>.
- Perkins-Kirkpatrick, S. E. & Lewis, S. C. Increasing trends in regional heatwaves. *Nat. Commun.* **11**, 3357 (2020).
- Rousi, E. et al. Accelerated western European heatwave trends linked to more-persistent double jets over Eurasia. *Nat. Commun.* **13**, 3851 (2022).
- Bevacqua, E. et al. Precipitation trends determine future occurrences of compound hot–dry events. *Nat. Clim. Change* **12**, 350–355 (2022).
- Kornhuber, K. et al. Risks of synchronized low yields are underestimated in climate and crop model projections. *Nat. Commun.* **14**, 3528 (2023).
- Zscheischler, J. & Seneviratne, S. I. Dependence of drivers affects risks associated with compound events. *Sci. Adv.* **3**, e1700263 (2017).
- Manning et al. Increased probability of compound long-duration dry and hot events in Europe during summer (1950–2013). *Environ. Res. Lett.* **14**, 094006 (2019).
- Park, H.-S., Lee, S., Son, S.-W., Feldstein, S. B. & Kosaka, Y. The impact of poleward moisture and sensible heat flux on Arctic winter sea ice variability. *J. Clim.* **28**, 5030–5040 (2015).
- Jiang, S., Bevacqua, E. & Zscheischler, J. River flooding mechanisms and their changes in Europe revealed by explainable machine learning. *HESS* **26**, 6339–6359 (2022).
- Shi, Z., Jia, G., Zhou, Y., Xu, X. & Jiang, Y. Amplified intensity and duration of heatwaves by concurrent droughts in China. *Atmos. Res.* **261**, 105743 (2021).
- Zscheischler, J. et al. A typology of compound weather and climate events. *Nat. Rev. Earth Environ.* **1**, 333–347 (2020).
- Brutsaert, W. On a derivable formula for long-wave radiation from clear skies. *Water Resour. Res.* **11**, 742–744 (1975).
- Ghausi, S. A., Tian, Y., Zehe, E. & Kleidon, A. Radiative controls by clouds and thermodynamics shape surface temperatures and turbulent fluxes over land. *Proc. Natl Acad. Sci. USA* **120**, e2220400120 (2023).
- Tian, Y. et al. Understanding variations in downwelling longwave radiation using Brutsaert’s equation. *Earth Syst. Dyn.* **14**, 1363–1374 (2023b).
- Hersbach, H. et al. The ERA5 global reanalysis. *Q. J. R. Meteorol. Soc.* **146**, 1999–2049 (2020).

32. Jung, M. et al. Compensatory water effects link yearly global land CO₂ sink changes to temperature. *Nature* **541**, 516–520 (2017).
33. Tramontana, G. et al. Predicting carbon dioxide and energy fluxes across global FLUXNET sites with regression algorithms. *Biogeosciences* **13**, 4291–4313 (2016).
34. Portmann, F. T., Siebert, S. & Döll, P. MIRCA2000—Global monthly irrigated and rainfed crop areas around the year 2000: A new high-resolution data set for agricultural and hydrological modeling. *Global Biogeochem. Cycles* **24**, GB1011 (2010).
35. Center for International Earth Science Information Network - CIESIN - Columbia University. 2018. Gridded Population of the World, Version 4 (GPWv4); Population Density Adjusted to Match 2015 Revision UN WPP Country Totals, Revision 11. (Palisades, New York: NASA Socioeconomic Data and Applications Center (SEDAC); accessed 1 October 2023) <https://doi.org/10.7927/H4F47M65>.
36. Luo, M. et al. Two different propagation patterns of spatiotemporally contiguous heatwaves in China. *NPJ Clim. Atmos. Sci.* **5**, 89 (2022).
37. Lee, S. et al. Revisiting the Cause of the 1989–2009 Arctic surface warming using the surface energy budget: downward infrared radiation dominates the surface fluxes. *Geophys. Res. Lett.* **44**, 10,654–10,661 (2017).
38. Zeppetello, L. R. V. et al. Identifying the sources of continental summertime temperature variance using a diagnostic model of land–atmosphere interactions. *J. Clim.* **33**, 3547–3564 (2020).
39. Pedregosa et al., Scikit-learn: Machine Learning in Python, *JMLR* **12**, 2825–2830, (2011). https://scikit-learn.org/stable/auto_examples/cluster/plot_kmeans_silhouette_analysis.html
40. Rousseeuw, P. J. Silhouettes – A graphical aid to the interpretation and validation of cluster-analysis. *J. Comput. Appl. Math.* **20**, 53–65 (1987).
41. Lesk, C., Rowhani, P. & Ramankutty, N. Influence of extreme weather disasters on global crop production. *Nature* **529**, 84–87 (2016).

Acknowledgements

This research resulted from a research stay of YT in JZ's research group supported by Helmholtz Information & Data Science Academy (HIDA) Visiting Researcher Grant as No. 14679 and in AK's research group supported by China Scholarship Council as No. 202106210161. The authors would like to acknowledge Topology of Hydrosphere Project supported by Key Laboratory of Hydrosphere Sciences of the Chinese Ministry of Water Resources (grant no. sklhse-TD-2024-F01, DZ), European Union's Horizon 2020 research and innovation programme under grant agreement No 101003469 (JZ), the Helmholtz Initiative and Networking Fund (Young Investigator Group COMPOUNDX, Grant 6Agreement VH-NG-1537, JZ), and the ClimXtreme project subprojects PERSEVERE supported by the German Federal Ministry of Education and Research (grant no. 01LP2322D, YT). The authors also benefited from the discussion with Dr. Emanuele Bevacqua, Dr. Beijing Fang from the Department of Computational Hydrosystems, Helmholtz Centre for Environmental Research (UFZ), and Ms. Sifang Feng from Beijing Normal University (BNU).

Author contributions

Y.T. led the conceptualization, methodology development, investigation, visualization, and writing of the original draft, as well as contributed to the review and editing. A.K. contributed to the conceptualization and methodology development. C.L. assisted with methodology development and contributed to the review and editing. S.Z. played a role in reviewing and editing the manuscript. X.L. contributed to the review and editing process. S.A.G. supported the investigation phase of the study. G.W. provided supervision throughout the research and led the project. D.Z. contributed to the conceptualization, supervision, and review of the work. J.Z. played a central role in the conceptualization, methodology development, investigation, supervision, and editing.

Funding

Open Access funding enabled and organized by Projekt DEAL.

Competing interests

The authors declare no competing interests.

Additional information

Supplementary information The online version contains supplementary material available at <https://doi.org/10.1038/s43247-024-01784-y>.

Correspondence and requests for materials should be addressed to Deyu Zhong or Jakob Zscheischler.

Peer review information *Communications Earth & Environment* thanks the anonymous reviewers for their contribution to the peer review of this work. Primary Handling Editors: Alireza Bahadori and Jialiang Cai. A peer review file is available.

Reprints and permissions information is available at <http://www.nature.com/reprints>

Publisher's note Springer Nature remains neutral with regard to jurisdictional claims in published maps and institutional affiliations.

Open Access This article is licensed under a Creative Commons Attribution 4.0 International License, which permits use, sharing, adaptation, distribution and reproduction in any medium or format, as long as you give appropriate credit to the original author(s) and the source, provide a link to the Creative Commons licence, and indicate if changes were made. The images or other third party material in this article are included in the article's Creative Commons licence, unless indicated otherwise in a credit line to the material. If material is not included in the article's Creative Commons licence and your intended use is not permitted by statutory regulation or exceeds the permitted use, you will need to obtain permission directly from the copyright holder. To view a copy of this licence, visit <http://creativecommons.org/licenses/by/4.0/>.

© The Author(s) 2024